

The analysis of crack tip fields in ferroelastic materials

Dorinamaria Carka and Chad M Landis¹

The University of Texas at Austin, Department of Aerospace Engineering and Engineering Mechanics, 210 East 24th Street, C0600, Austin, TX 78712-0235, USA

E-mail: landis@mail.utexas.edu

Received 31 January 2011, in final form 1 April 2011

Published 30 August 2011

Online at stacks.iop.org/SMS/20/094005

Abstract

The stress and strain fields near a stationary crack in a ferroelastic material are analyzed. The constitutive response of the material is taken to be characteristic of a polycrystalline sample assembled from randomly oriented tetragonal single crystal grains. The constitutive law accounts for the strain saturation, asymmetry in tension versus compression, Bauschinger effects, reverse switching, and strain reorientation that can occur in these materials due to the non-proportional loading that can arise near a crack tip. Detailed finite element calculations are carried out to determine the stress and strain fields in the vicinity of the crack tip, and to compute values for the J -integral on various integration paths around the tip. The results of the calculations are discussed in relation to results for growing cracks and for stationary cracks in standard elastic-plastic materials.

(Some figures in this article are in colour only in the electronic version)

1. Introduction

The understanding of the fracture properties of ferroelectric/ferroelastic ceramics is as yet incomplete. There have been many excellent experimental and theoretical investigations on the fracture properties of ferroelectrics, recently summarized by Schneider (2007) and Kuna (2010). To model the effects of domain switching Yang and Zhu (1998) and Reece and Guiu (2002) followed the approaches of McMeeking and Evans (1982) and Budiansky *et al* (1983) for transformation toughening in materials undergoing a dilatant phase transformation. These models assume that a given material point consists of a single domain variant and switching between variants is driven by an energetic criterion, e.g. Kessler and Balke (2001). Such a description of the material is physically correct, but to fully model a ferroelectric in this manner would require the tracking of the locations and interactions of many domain walls. To carry out such a program for millimeter to centimeter sized samples of material would be computationally intensive.

A second approach taken by Landis (2003b), Wang and Landis (2004, 2006) is to implement a phenomenological

constitutive law to describe ferroelastic/ferroelectric switching within detailed finite element computations of the electromechanical fields around the crack tip. In contrast to the transformation-type switching model, a material point can contain multiple domain variants. To date such calculations have been performed on growing cracks to determine the amount of toughening that is provided by domain switching during crack growth. Some of the successes of this approach include the prediction of switching zones with a gradation of switching strain and similar R -curve toughening enhancements for both unpoled material and the same material poled parallel to the crack front as observed by Hackemann and Pfeiffer (2003) and Jones *et al* (2007). In this work a phenomenological constitutive law is used to study the mechanical fields near a stationary crack tip in a ferroelastic material.

The remainder of the paper is organized as follows. Section 2 presents the constitutive law used to describe polycrystalline ferroelastic materials. Section 3 presents the crack tip computations along with interesting results for the path-dependence of the J -integral around stationary cracks in ferroelastic materials. Finally, section 4 will be used to discuss the results in relation to their steady crack growth counterparts.

¹ Address for correspondence: 210 East 24th Street, C0600, Austin, TX 78712-0235, USA.

2. Constitutive law for ferroelastic switching

The nonlinear constitutive response of ferroelastic ceramics is a result of the mechanism of domain switching. A more detailed discussion of domain switching and the constitutive behavior of ferroelectric and ferroelastic materials can be found in Huber *et al* (1999), Kamlah (2001), or Landis (2004). Here we are interested in the behavior of ferroelastic polycrystals and a phenomenological constitutive description that can be readily implemented within finite element computations. Such a model has been developed by Landis (2003a), which is a special case of the more general model for ferroelectrics, Landis (2002).

For completeness the constitutive equations are reviewed here. First, isotropic elastic response and linear kinematics is assumed such that the stress–strain relations are written as

$$\varepsilon_{ij} = \frac{1+\nu}{E}\sigma_{ij} - \frac{\nu}{E}\sigma_{kk}\delta_{ij} + \varepsilon_{ij}^r. \quad (2.1)$$

Here, ε_{ij} , ε_{ij}^r and σ_{ij} are the Cartesian components of the infinitesimal strain tensor, the remanent strain tensor and the Cauchy stress tensor, ν is the Poisson's ratio and E is the Young's modulus. In all cases discussed in this paper, the datum for remanent strain is the state of the material as cooled from above the Curie temperature.

The purpose of the nonlinear constitutive law is to provide the evolution of the remanent strain history given the stress or total strain history. Consistent with the facts that domain switching gives rise to deviatoric strains and ferroelastic ceramics exhibit kinematic hardening effects, it is assumed that the material responds elastically within a switching surface Φ described by

$$\Phi = \frac{3}{2}\left(s_{ij} - s_{ij}^B\right)\left(s_{ij} - s_{ij}^B\right) - \sigma_0^2 = 0. \quad (2.2)$$

Here s_{ij} are the components of the stress deviator such that $s_{ij} = \sigma_{ij} - \delta_{ij}\sigma_{kk}/3$, s_{ij}^B are the components of the deviator of the back stress tensor σ_{ij}^B , σ_0 is the initial switching (yield) strength of the material in tension or compression. If the stress state is on the switching surface and the load increment induces remanent straining, then the remanent strain increment is normal to the switching surface such that

$$\dot{\varepsilon}_{ij}^r = \lambda(s_{ij} - s_{ij}^B), \quad (2.3)$$

where λ is the plastic multiplier.

The back stress tensor leads to kinematic hardening and must be used to enforce the remanent strain saturation conditions. The approach used to determine the back stresses is based on the assumption that the internal state of the ferroelastic material is completely characterized by the components of the remanent strain tensor, Cocks and McMeeking (1999) and Landis (2002). This assumption leads to the identification of a remanent potential, $\Psi^r(\varepsilon_{ij}^r)$, such that the back stresses are derived from the potential in the following manner

$$\sigma_{ij}^B = \frac{\partial \Psi^r}{\partial \varepsilon_{ij}^r}. \quad (2.4)$$

In order to complete the constitutive theory, the form of Ψ^r must be specified. As previously noted, ferroelectric ceramics exhibit an asymmetry in the attainable levels of remanent strain in tension versus compression. The micromechanical simulations of Frölich (2001), Landis (2003a) and Landis *et al* (2004) suggest that in random polycrystals with underlying tetragonal crystal structure, the ratio of remanent strain possible in tension to that possible in compression is 1.37:1. This theoretical value is in the same range as the ratio of the maximum poling remanent strain to the maximum compressive remanent strain due to stress depolarization measured in PLZT by Lynch (1996), and in PZT by Fang and Li (1999).

By implementing the micromechanical model of Huber *et al* (1999), Landis (2003a) determined the full range of remanent strain saturation states. The following procedure is used to determine when saturation is approached. First, since the remanent strain due to domain switching is volume conserving, the following two remanent strain invariants are used to describe any multi-axial remanent strain state.

$$J_2^e = (\frac{2}{3}\varepsilon_{ij}^r\varepsilon_{ij}^r)^{1/2} \quad \text{and} \quad J_3^e = (\frac{4}{3}\varepsilon_{ij}^r\varepsilon_{jk}^r\varepsilon_{ki}^r)^{1/3}. \quad (2.5)$$

Here, ε_{ij}^r is the remanent strain deviator, $\varepsilon_{ij}^r = \varepsilon_{ij}^r - \delta_{ij}\varepsilon_{kk}^r/3$. With the definition of these two invariants, a full range of remanent strain saturation states can be probed by allowing the ratio of J_3^e/J_2^e to vary from -1 (axisymmetric contraction) to 0 (pure shear) to 1 (axisymmetric extension).

Next, the strain-like variable $\bar{\varepsilon}$ is defined as

$$\bar{\varepsilon} = J_2^e f\left(J_3^e/J_2^e\right) \quad (2.6)$$

where

$$f\left(\frac{J_3^e}{J_2^e}\right) = -0.0965\left(\frac{J_3^e}{J_2^e}\right)^3 + 0.01\left(\frac{J_3^e}{J_2^e}\right)^6 + 0.8935, \quad \text{for } \left(\frac{J_3^e}{J_2^e}\right) < 0 \quad (2.7)$$

and

$$f\left(\frac{J_3^e}{J_2^e}\right) = -0.1075\left(\frac{J_3^e}{J_2^e}\right)^3 - 0.027\left(\frac{J_3^e}{J_2^e}\right)^6 - 0.028\left(\frac{J_3^e}{J_2^e}\right)^{21} + 0.8935, \quad \text{for } \left(\frac{J_3^e}{J_2^e}\right) \geq 0. \quad (2.8)$$

Here, f is a functional fit to the numerical results obtained from micromechanical computations. When the remanent strain level characterized by $\bar{\varepsilon}$ reaches the compressive saturation level, ε_c , the remanent strain will be saturated. In other words, the only possible remanent strain states in the material are those that satisfy $\bar{\varepsilon} \leq \varepsilon_c$. In order to prohibit remanent strain states characterized by $\bar{\varepsilon} > \varepsilon_c$, the remanent potential Ψ^r is constructed to increase without bound as $\bar{\varepsilon} \rightarrow \varepsilon_c$.

The simple functional form of the remanent potential that has been chosen for this fracture study is,

$$\Psi^r = \frac{1}{2}H_0\varepsilon_c \left[\frac{J_2^e}{\varepsilon_c} \exp\left(\frac{m}{1 - \bar{\varepsilon}/\varepsilon_c}\right) \right]^2. \quad (2.9)$$

H_0 is a characteristic level of back stress that primarily affects the initial slope of the uniaxial stress versus remanent

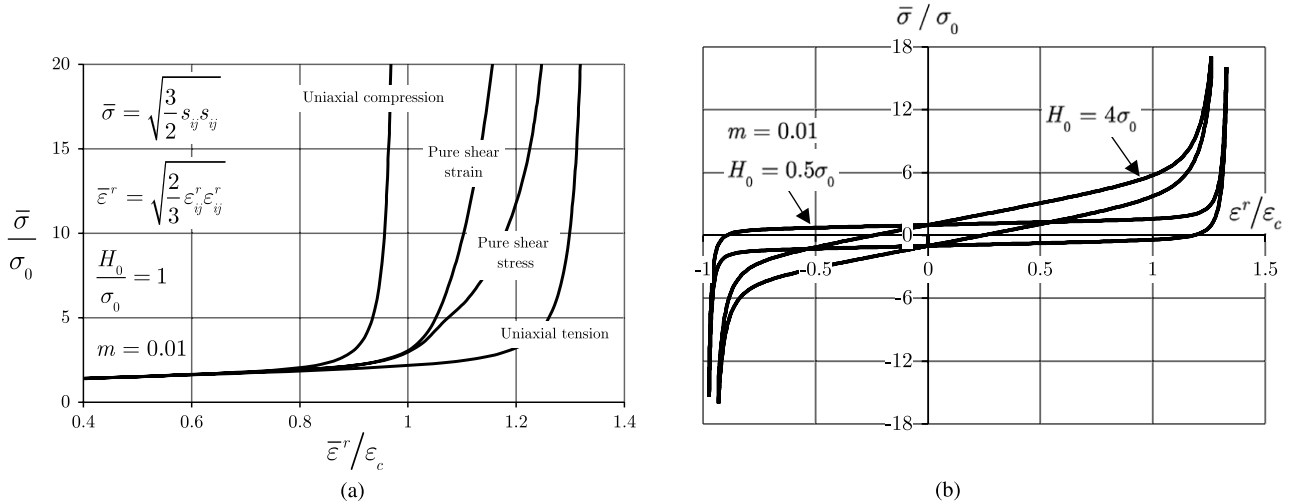


Figure 1. (a) Effective stress versus effective remanent strain curves for the model material described in section 2 in uniaxial compression, pure shear strain, pure shear stress and uniaxial tension tests. (b) Uniaxial stress versus remanent strain hysteresis loops for the model material illustrating the effect of the hardening parameter H_0 . In both cases notice the asymmetry in the remanent strains that can be achieved in tension versus compression.

strain curve, and m is another hardening parameter that controls how abruptly the strain saturation conditions are reached. Figure 1(a) illustrates the predictions of the effective stress versus the effective remanent strain from the constitutive law for uniaxial compression, pure shear strain, pure shear stress and uniaxial tension. Note that the shear strain and shear stress curves do not coincide. This behavior is due to the fact that the material can strain more in tension than in compression, and has been confirmed in micromechanical simulations. This feature of the constitutive behavior also has consequences for the remanent strain fields near crack tips in mode II loading. Figure 1(b) illustrates the uniaxial stress versus remanent strain hysteresis curves for a few different sets of the material parameters H_0 and m .

The constitutive model is now completely specified, and can be used to compute remanent strain histories. For the finite element computations a backward Euler method is implemented to integrate the constitutive model, and consistent tangent moduli have been derived for the plane strain cases studied.

3. Crack tip field computations

For the computations of the crack tip fields, it is assumed that the applied loading is small such that the maximum radial dimension of the switching zone around the crack is much smaller than the length of the crack or any other specimen length dimension. As discussed by Rice (1968), under these conditions a small scale switching analysis can be performed on a semi-infinite crack with the remote applied stress field being that of the asymptotic elastic K -fields,

$$\begin{aligned} \left\{ \begin{array}{l} \sigma_{11} \\ \sigma_{22} \\ \sigma_{12} \end{array} \right\} &= \frac{K_I}{\sqrt{2\pi r}} \cos \frac{\theta}{2} \left\{ \begin{array}{l} 1 - \sin \frac{\theta}{2} \sin \frac{3\theta}{2} \\ 1 + \sin \frac{\theta}{2} \sin \frac{3\theta}{2} \\ \sin \frac{\theta}{2} \cos \frac{3\theta}{2} \end{array} \right\} \\ &+ \frac{K_{II}}{\sqrt{2\pi r}} \left\{ \begin{array}{l} \sin \frac{\theta}{2} (-2 + \cos \frac{\theta}{2} \cos \frac{3\theta}{2}) \\ \sin \frac{\theta}{2} \cos \frac{\theta}{2} \cos \frac{3\theta}{2} \\ \cos \frac{\theta}{2} (1 - \sin \frac{\theta}{2} \sin \frac{3\theta}{2}) \end{array} \right\} \text{ as } r \rightarrow \infty. \quad (3.1) \end{aligned}$$

Here K_I and K_{II} are the remote applied mode I and mode II stress intensities and r and θ are polar coordinates centered on the crack tip. In order to apply these remote boundary conditions a Dirichlet to Neumann (DtN) map technique is used as described in Carka *et al* (2011). The DtN map allows for the exact application of the remote boundary conditions, and it also allows for all of the finite element degrees of freedom to be used solely in the vicinity of the crack tip where the interesting constitutive processes are occurring without wasting any computational effort by attempting to model an infinite region with a large but finite domain.

Under plane strain conditions an approximation for the characteristic size of this switching zone, R_s , is given as

$$R_s = \frac{1}{3\pi} \frac{K_I^2 + \frac{25}{4}K_{II}^2}{\sigma_0^2}. \quad (3.2)$$

In section 3.1 a more detailed discussion of the size and shape of the plastic zone in both mode I and mode II loading will be presented. In addition to the stress, strain and remanent strain fields near the crack tip, values for the J -integral, Rice (1968), are also computed on several circular contours centered on the crack tip.

$$J = \int_{\Gamma} (W n_1 - \sigma_{ji} n_j u_{i,1}) d\Gamma, \quad (3.3)$$

where Γ is a counterclockwise directed contour encircling the crack tip, n_i are the components of the unit normal directed to the right along the contour, u_i are the components of the displacement vector, and W is the strain-history-dependent stress work density at a material point defined by

$$W = \int_0^{\varepsilon} \sigma_{ij} d\varepsilon_{ij}. \quad (3.4)$$

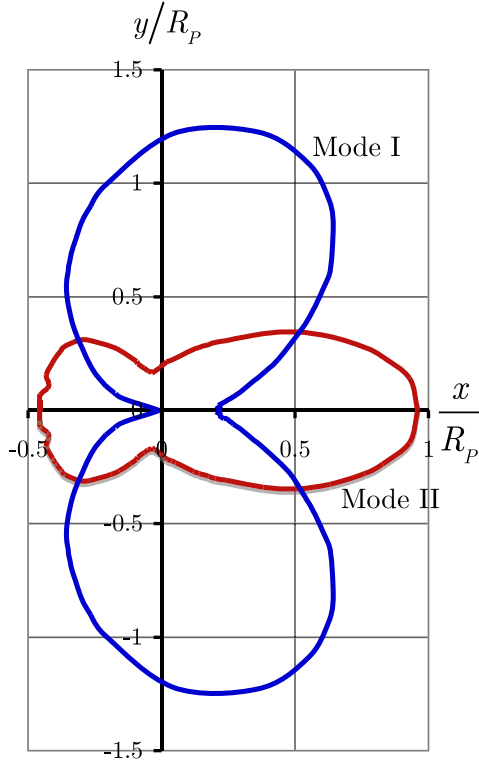


Figure 2. The sizes and shapes of the switching zone boundaries for mode I and mode II loading or $H/\sigma_0 = 1$ and $E\varepsilon_c/\sigma_0 = 5$.

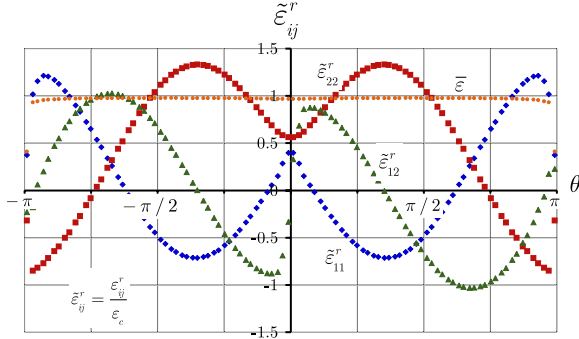


Figure 3. Angular variation of the remanent strains close to the crack tip for mode I loading and material parameters $H/\sigma_0 = 1$, $E\varepsilon_c/\sigma_0 = 5$, $\nu = 0.3$.

In this work the J -integral is computed using the domain integral technique of Li *et al* (1985).

$$J_A = - \int_A (W q_{,1} - \sigma_{j,i} q_{,j} u_{i,1}) dA. \quad (3.5)$$

Here A is an area that contains both the top and bottom crack faces as part of its boundary. For the calculations in here A will be a circular annulus with inner radius R_i and outer radius R_o . For nonlinear elastic materials J is path-independent and $J_A = J$ for any q that is unity along the inner boundary of A and zero along its outer boundary. Carka and Landis (2011) showed that, for cases where J is path-dependent, by selecting the function q as,

$$q = \frac{r - R_o}{R_i - R_o} \rightarrow q_{,j} = \frac{r_{,j}}{R_i - R_o} = \frac{n_j}{R_i - R_o}, \quad (3.6)$$

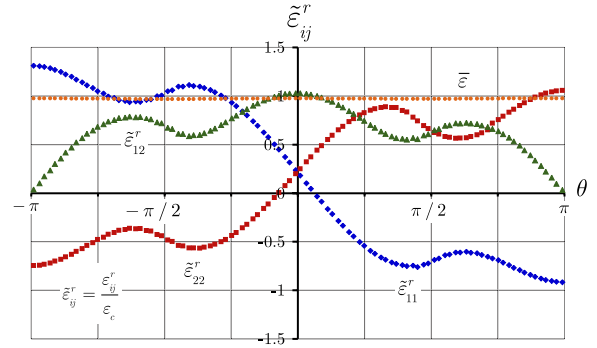


Figure 4. Angular variation of the remanent strains close to the crack tip for mode II loading and material parameters $H/\sigma_0 = 1$, $E\varepsilon_c/\sigma_0 = 5$, $\nu = 0.3$.

then J_A is equal to the radial average of J for all circular paths in A .

Within this model dimensional analysis dictates that all field quantities, for example the stresses, will be of the form

$$\frac{\sigma_{ij}}{\sigma_0} = \bar{\sigma}_{ij} \left(\frac{x}{R_s}, \frac{y}{R_s}; \frac{E_c E}{\sigma_0}, \frac{H_0}{\sigma_0}, m, \nu \right), \quad (3.7)$$

where $\bar{\sigma}_{ij}$ are dimensionless functions of the normalized spatial coordinates parameterized by the normalized material quantities. Also note that here R_s is the characteristic size of the switching zone given by equation (3.2). Additionally the J -integral will only depend on the dimensionless material parameters and the radial size of the integration contour, $r = (R_i + R_o)/2$,

$$\frac{J}{J_\infty} = \bar{J} \left(\frac{r}{R_s}; \frac{E_c E}{\sigma_0}, \frac{H_0}{\sigma_0}, m, \nu \right). \quad (3.8)$$

3.1. Results

The numerical calculations for a plane strain stationary crack presented in this section are performed employing a full circular mesh for the mode II loading. Taking into consideration the symmetry in mode I, only half of the mesh is considered. For all of the calculations to be presented the Poisson's ratio is taken to be $\nu = 0.3$ and the hardening exponent parameter is $m = 0.01$. Figure 2 illustrates the shapes of the plastic zones for mode I and mode II loading for, $H/\sigma_0 = 1$ and $E\varepsilon_c/\sigma_0 = 5$. The K -field loading specifying the size of the zone is given by equation (3.3) for all calculations. The effect of the parameter H/σ_0 on the shape of the zones is similar to the effect the hardening exponent has on the shape of plastic zones for elastic power law hardening materials, see Carka and Landis (2011). As H/σ_0 increases, the mode I zone shape becomes increasingly symmetric with respect to the y -axis. The mode II zone shrinks ahead of the crack tip and expands along the crack faces. The effect of $E\varepsilon_c/\sigma_0$ on the shape of the zones is much less pronounced but increasing the value of the ratio leads to an overall smaller size of the switching zone.

Figures 3 and 4 show the angular variation of the remanent strain components in the elements surrounding the crack tip for mode I and mode II loading respectively. All the quantities

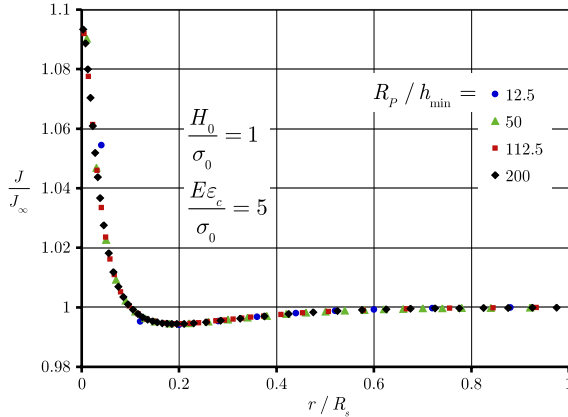


Figure 5. The J -integral versus the radius of the circular integration contour for mode I loading. The different markers refer to different applied loading levels from the same simulation illustrating the self-similarity of the solution.

plotted are normalized by the compressive saturation strain. The variable $\bar{\epsilon}$, which describes the multi-axial saturation behavior is near its saturation limit of ε_c for almost all angles around the crack tip in both loading modes. The stress variation is very similar to the findings in Landis (2003b). An elastic $1/\sqrt{r}$ singularity is recovered at the crack tip since this region close to the tip is very close to saturation, but the angular variation of the stresses differs slightly from the purely elastic asymptotic field. Notice in figure 4 that the axial remanent strain components are not equal to zero on the plane ahead of the crack tip even though, due to considerations of the mode II symmetry, the axial stresses on this plane are zero. This is a consequence of the tension–compression asymmetry in the strain saturation that is manifested in figure 1 as a difference in the constitutive responses in pure shear stress versus pure shear strain.

Next, we proceed in the presentation of a quite interesting feature of the path-dependence of the J -integral in ferroelastic

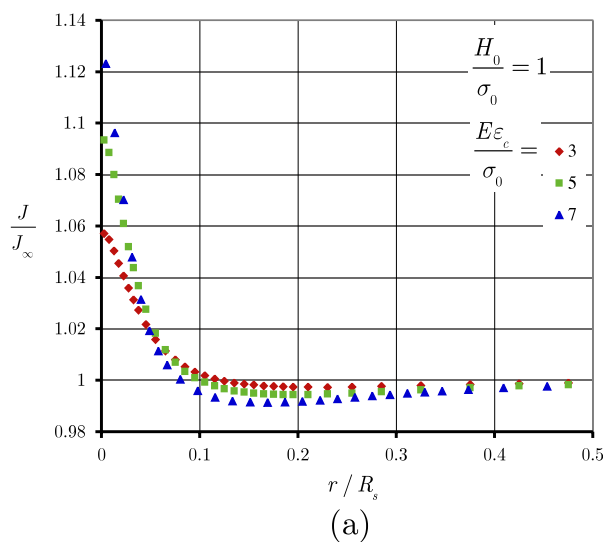
materials. The J -integral, calculated on paths that do not intersect the switching zone is related to the applied far-field K loading through

$$J_\infty = \frac{1 - v^2}{E} (K_I^2 + K_{II}^2). \quad (3.9)$$

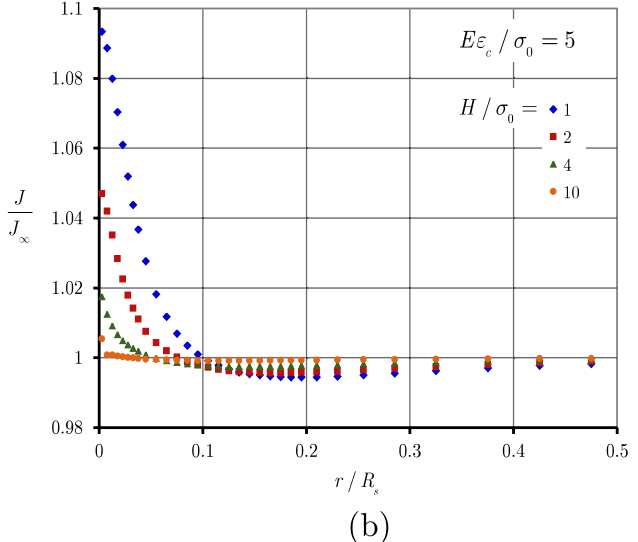
Figure 5 shows the variation of the J -integral normalized by the far-field applied J_∞ for different circular paths around the crack tip at different levels of the applied mode I loading. The far-field loading is applied in 400 increments and the J -integral is computed along all circular paths at every 100 increments. These four loading levels correspond to sizes of the switching zones which are 12.5, 50, 112.5 and 200 times larger than the radial extend of the crack tip ring of elements h_{\min} , indicating the amount of numerical refinement that exists at each of these load levels. Figure 5 indicates that the self-similarity of the solution is well established after 200 increments. Note that all of the integration paths reported in the figure lie either entirely within or at least intersect the switching the zone.

It is interesting to note that for r/R_s between 0.2 and 1, the J -integral follows the behavior of an elastic–perfectly plastic material without saturation, although the actual amount of the path-dependence differs by approximately 3% compared with similar calculation given in Carka and Landis (2011). It can be argued that the path-dependence in this region is not significant, but it does contrast the rising behavior as the integration contour becomes more deeply embedded within the switching zone where the material surrounding the tip is strain-saturated. The rising value of the J -integral eventually reaches approximately 9% above the applied value at the crack tip for $H/\sigma_0 = 1$ and $E\varepsilon_c/\sigma_0 = 5$. Figures 6(a) and (b) illustrate the effects of the saturation strain $E\varepsilon_c/\sigma_0$ and the hardening parameter H/σ_0 on the path-dependence of the J -integral in mode I loading.

Also of interest is the behavior of the path-dependence for pure mode II loading especially when compared to elastic–perfectly plastic case. The calculations in Carka and Landis



(a)



(b)

Figure 6. The J -integral versus the radius of the circular integration contour for mode I loading for (a) different levels of the saturation strain $E\varepsilon_c/\sigma_0$ and (b) different levels of the hardening parameter H/σ_0 .

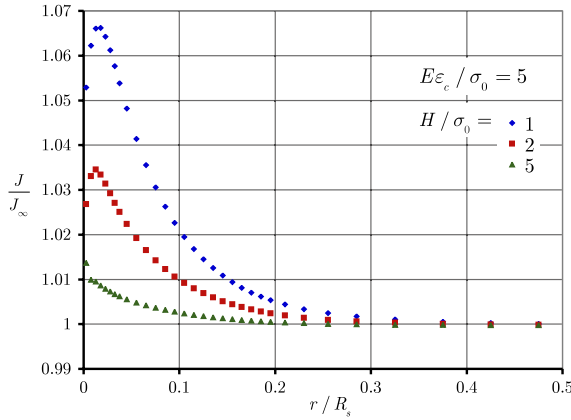


Figure 7. The J -integral versus the radius of the circular integration path for mode II loading and different values of H/σ_0 .

(2011) demonstrate that the significant path-dependence of the J -integral in mode I practically disappears for mode II loading of a crack in an elastic–perfectly plastic material. Figure 7 shows that this is not the case for ferroelastic materials.

Figure 7 shows the path-dependence of the J -integral for $E\varepsilon_c/\sigma_0 = 5$ and three different hardening parameters for mode II loading. It can be seen that for $r/R_p > 0.3$ the J -integral mimics the path-independent behavior of the elastic–perfectly plastic case. However, as the crack tip is approached the increase of J as seen in the mode I case appears with the J -integral at the tip being about 5% more than the far-field value. Note that for mode II the tip value is not the maximum value of the J -integral which occurs away from the tip.

As discussed in Landis (2003b), the material parameters H/σ_0 and $E\varepsilon_c/\sigma_0$ have a strong effect on the fracture toughness enhancement in ferroelastic ceramics during steady crack growth. These parameters also affect the path-dependence of J presented in this work for stationary cracks. The stress required to create a specific amount of remanent strain increases with increasing H/σ_0 . On the other hand increasing values of $E\varepsilon_c/\sigma_0$ implies stress relaxation since the material is able to accommodate more irreversible strain. Figure 8 presents the effect of these parameters on the value of the J integral at the crack tip for mode I loading. The difference between the J -integral at the tip and the far-field applied value is most pronounced for low values of H/σ_0 and increases with increasing $E\varepsilon_c/\sigma_0$. For $H/\sigma_0 = 1$ the deviation from the far-field value is about 5% when $E\varepsilon_c/\sigma_0 = 3$ and 12% for $E\varepsilon_c/\sigma_0 = 7$. The path-dependence of the J -integral becomes less significant for high values of H/σ_0 and the effect of $E\varepsilon_c/\sigma_0$ on J is reduced for large H/σ_0 .

4. Discussion

In this work we have refrained from explicitly stating a fracture criterion for ferroelastic material. One physically rational criterion for crack growth initiation from a stationary crack would be that crack growth begins when the crack tip energy release rate is equal to a material specific critical energy release rate, i.e. $\mathcal{G}_{\text{tip}} = \mathcal{G}_c$. Note that due to the path-dependence of the J -integral it is necessary to identify the crack tip energy release rate $\mathcal{G}_{\text{tip}} = J_{\text{tip}}$ since this quantity will not be equal

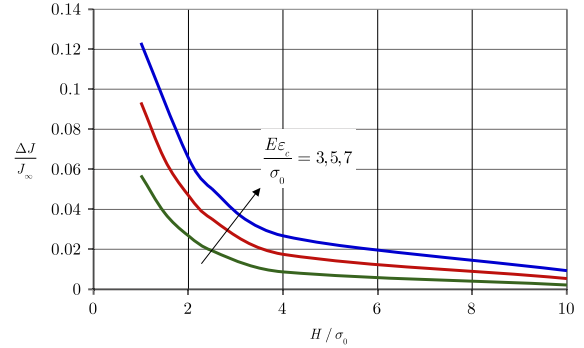


Figure 8. The dependence of the crack tip value of the J -integral on H/σ_0 and $E\varepsilon_c/\sigma_0$ for mode I loading.

to the applied energy release rate, $\mathcal{G}_{\text{applied}} = J_\infty$. In fact, our calculations have demonstrated that, with respect to the energy release rate, the domain switching zone around the crack tip causes anti-shielding. This is in contrast to transformation-type switching models, which predict neither shielding nor anti-shielding due to switching near a stationary crack.

It is also interesting to note that the material parameters that lead to the greatest levels of anti-shielding around a stationary crack, small H/σ_0 and large $E\varepsilon_c/\sigma_0$, cause the greatest amount of shielding for a growing crack, see Landis (2003b). However, it should be realized that the anti-shielding around a stationary crack is on the order of 10%, while the shielding around a steadily growing crack is 100%–200%. Nevertheless, the crack growth initiation toughness can have a marked effect on fracture loads depending on the initial slope of the R -curve.

The point fracture criterion $\mathcal{G}_{\text{tip}} = \mathcal{G}_c$ should be used with considerable caution. While reasonable on the surface this criterion does come with certain embedded assumptions. Specifically, this criterion assumes that the material can sustain a singularity such that the constitutive law being used is valid in the entire domain. Clearly this assumption must break down at some point, but this alone does not invalidate the point fracture criterion. A more realistic fracture criterion would be to introduce a fracture process or cohesive zone to represent the actual material separation mechanics. Typically such cohesive traction separation laws are characterized by a cohesive strength σ_c and a cohesive energy \mathcal{G}_c . One can imagine that these parameters can be vastly different depending on the separation mechanics with atomic cleavage having a high σ_c and low \mathcal{G}_c and grain pullout having a smaller σ_c but larger \mathcal{G}_c . A rough calculation of the distance ahead of the crack where cohesive tractions play an important role is $R_c = \mathcal{G}_c E/\sigma_c^2$. Now if this cohesive length scale is small compared to the strain saturation region predicted by the present model ($R_{\text{sat}} \approx R_s/10$) then a point fracture criterion is valid. If the region where cohesive tractions play a role is comparable to the size of the strain saturation zone, then the point fracture criterion can no longer be valid because the reduction in stresses ahead of the crack tip due to the weak separation process will not allow the stresses to increase to the levels required for full strain saturation. This in turn will change the crack tip fields and the overall energy flux into the fracture process zone. For

weak fracture processes, like grain pullout, the present results suggest that a more detailed fracture model incorporating a cohesive zone are needed to gain a deeper understanding of ferroelastic fracture.

Acknowledgments

This work has been supported by the Army Research Office contract no. W911NF-07-1-0495 and NSF grant DMR-0909139.

References

- Budiansky B, Hutchinson J W and Lambropoulos J C 1983 Continuum theory of dilatant transformation toughening in ceramics *Int. J. Solids Struct.* **19** 337–55
- Carka D, Mear M E and Landis C M 2011 The Dirichlet-to-Neumann map for two-dimensional crack problems *Comput. Methods Appl. Mech. Eng.* **200** 1263–71
- Carka D and Landis C M 2011 On the path-dependence of the J -integral in an elastic–plastic material *J. Appl. Mech.* **78** 011006
- Cocks A C F and McMeeking R M 1999 A phenomenological constitutive law for the behavior of ferroelectrics *Ferroelectrics* **228** 219–28
- Fang D and Li C 1999 Nonlinear electric-mechanical behavior of a soft PZT-51 ferroelectric ceramic *J. Mater. Sci.* **34** 4001–10
- Frölich A 2001 Mikromechanisches modell zur ermittlung effektiver materialeigenschaften von piezoelektrischen polykristallen *Thesis* Universitat Karlsruhe, Germany
- Hackemann S and Pfeiffer W 2003 Domain switching in process zones of PZT: characterization by micro diffraction and fracture mechanical methods *J. Eur. Ceram. Soc.* **23** 141–51
- Huber J E, Fleck N A, Landis C M and McMeeking R M 1999 A constitutive model for ferroelectric polycrystals *J. Mech. Phys. Solids* **47** 1663–97
- Jones J L, Motahari S M, Varlioglu M, Lienert U, Bernier J V, Hoffman M and Ustundag E 2007 Crack tip process zone domain switching in a soft lead zirconate titanate ceramic *Acta Mater.* **55** 5538–48
- Kamlah M 2001 Ferroelectric and ferroelastic piezoceramics—modeling and electromechanical hysteresis phenomena *Contin. Mech. Thermodyn.* **13** 219–68
- Kessler H and Balke H J 2001 On the local and average energy release in polarization switching phenomena *J. Mech. Phys. Solids* **49** 953–78
- Kuna M 2010 Fract. mechanics of piezoelectric materials—Where are we right now? *Eng. Fract. Mech.* **77** 309–26
- Landis C M 2002 Fully coupled, multi-axial, symmetric constitutive laws for polycrystalline ferroelectric ceramics *J. Mech. Phys. Solids* **50** 127–52
- Landis C M 2003a On the strain saturation conditions for polycrystalline ferroelastic materials *J. Appl. Mech.* **70** 470–8
- Landis C M 2003b On the fracture toughness of ferroelastic materials *J. Mech. Phys. Solids* **51** 1347–69
- Landis C M 2004 Nonlinear constitutive modeling of ferroelectrics *Curr. Opin. Solid State Mater. Sci.* **8** 59–69
- Landis C M, Wang J and Sheng J 2004 Micro-electromechanical determination of the possible remanent strain and polarization states in polycrystalline ferroelectrics and implications for phenomenological constitutive theories *J. Intell. Mater. Syst. Struct.* **15** 513–25
- Li F Z, Shih C F and Needleman A 1985 A comparison of methods for calculating energy release rates *Eng. Fract. Mech.* **21** 405–21
- Lynch C S 1996 The effect of uniaxial stress on the electro-mechanical response of 8/65/35 PLZT *Acta Mater.* **44** 4137–48
- McMeeking R M and Evans A G 1982 Mechanics of transformation toughening in brittle materials *J. Am. Ceram. Soc.* **65** 242–6
- Reece M J and Guiu F 2002 Toughening produced by crack-tip-stress-induced domain reorientation in ferroelectric and/or ferroelastic materials *Phil. Mag. A* **82** 29–38
- Rice J R 1968 A path independent integral and the approximate analysis of strain concentration by notches and cracks *J. Appl. Mech.* **35** 379–86
- Schneider G A 2007 Influence of electric field and mechanical stress on the fracture of ferroelectrics *Ann. Rev. Mater. Res.* **37** 491–538
- Wang J and Landis C M 2004 On the fracture toughness of ferroelectric ceramics with electric field applied parallel to the crack front *Acta Mater.* **52** 3435–46
- Wang J and Landis C M 2006 Effects of in-plane electric fields on the toughening behavior of ferroelectric ceramics *J. Mech. Mater. Struct.* **1** 1075–95
- Yang W and Zhu T 1998 Switch toughening of ferroelectrics subjected to electric fields *J. Mech. Phys. Solids* **46** 291–311